Supplementary Information for:

Aqueous Eutectic Electrolytes Suppress Oxygen and Hydrogen Evolution for Long-Life Zn||MnO_2 Dual-Electrode-Free Batteries

Jinghan Li,[†a] Chang Li,[†*a], Bo Liu[b], Yuzhang Li[b], Oleg Borodin[c], Linda F. Nazar.*[a]

[a] Department of Chemistry and the Waterloo Institute for Nanotechnology, University of Waterloo, Ontario N2L 3G1, Canada

[b] Department of Chemical and Biomolecular Engineering, University of California, Los Angeles, California 90095, United States

[c] Battery Science Branch, Energy Science Division, DEVCOM Army Research Laboratory, Adelphi, Maryland 20783, United States

[†]These authors contributed equally.

Corresponding Authors:

*Chang Li: c553li@uwaterloo.ca

*Linda F. Nazar: lfnazar@uwaterloo.ca

Lead Contact Author:

Linda F. Nazar: lfnazar@uwaterloo.ca

Supplementary Figures

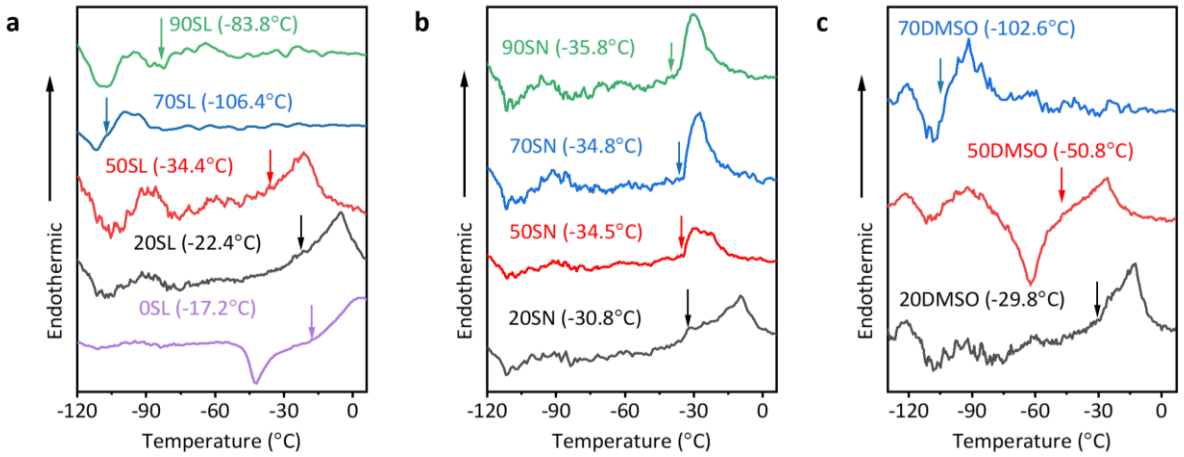

Supplementary Figure 1.
Differential scanning calorimetry results (DSC) results of electrolytes with different weight percentages of **a)** sulfolane (SL), **b)** dimethyl sulfoxide (DMSO) and **c)** succinonitrile (SN). The melting point is determined as the extrapolated onset temperature of the endothermic peak. No data is shown for 90DMSO as it does not dissolve the salt sufficiently. The electrolyte composition with the lowest melting point is selected. However, 70SN was chosen over 90SN due to the high viscosity of 90SN and the similar melting points of both compositions.

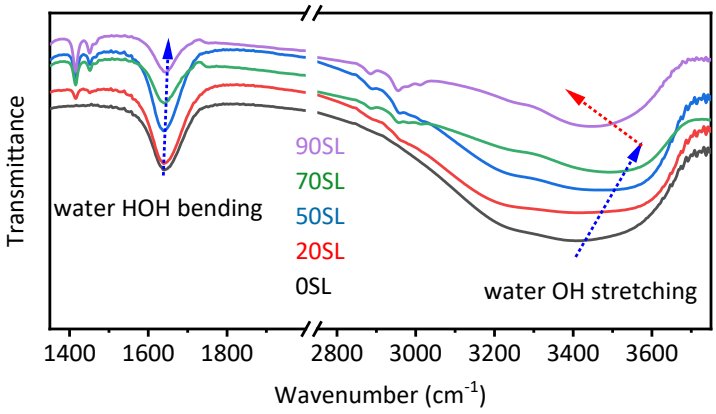

Supplementary Figure 2.
Fourier Transform Infrared Spectroscopy (FTIR) spectra for electrolytes with different sulfolane concentrations showing the initial red-shift at with increasing SL concentration, and then blue-shift in the -OH stretching region of 70SL.

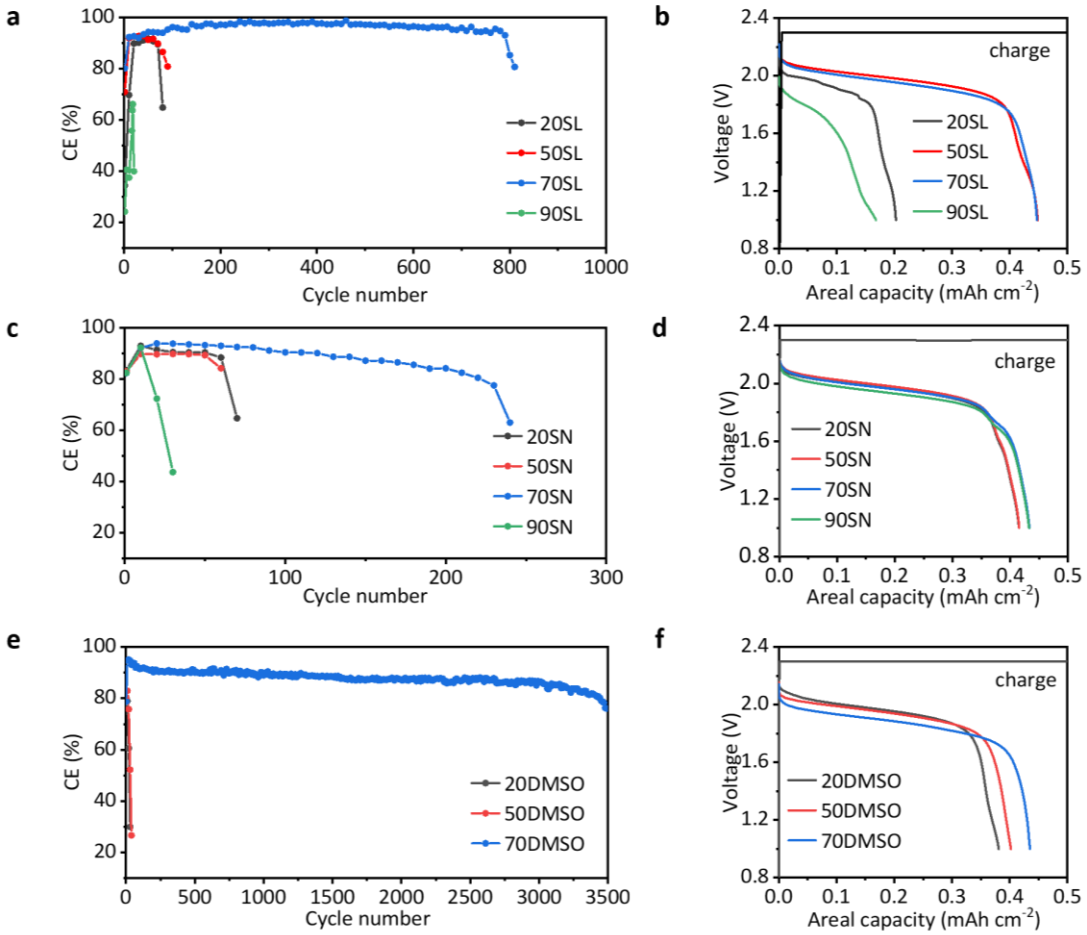

Supplementary Figure 3.
Electrochemical performance of $Zn^{2+}/Zn||MnO_2/Mn^{2+}$ cells in different electrolytes. **a, b**) Voltage profiles of full cells charged at 2.3 V for 0.5 mAh·cm^{-2} and galvanostatically discharged at 5 mA·cm^{-2} in different electrolytes and long-term cycling performance in electrolytes with different weight percentage of SL, **c, d**) SN, and **e, f**) DMSO. The electrolytes 50SL and 70SL demonstrated the highest discharge capacity, whereas 20SL and 90SL exhibited poor discharge performance (**Supplementary Fig. 3a** and **b**). While 0SL and 50SL also showed a high discharge capacity, they suffered from poor cycling stability compared to 70SL (**Supplementary Fig. 4**). For the SN/water system, 70SN demonstrated a longer cycling lifetime than the eutectic 90SN due to the former's lower viscosity and the similar melting points of both compositions (**Fig. S3c** and **d**). These results highlight the critical role of the organic solvent/water ratio in regulating MnO_2/Mn^{2+} redox activity, which results from the combined effect of viscosity, ionic conductivity (**Supplementary Fig. 5**) and the H-bonded network of water.

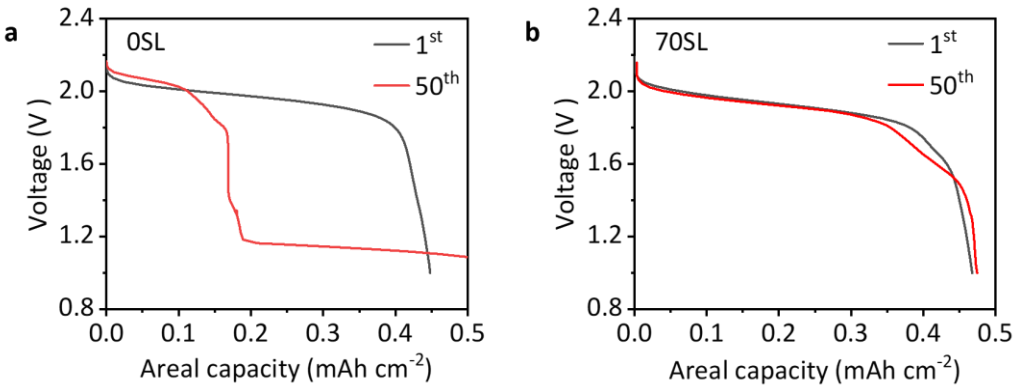

Supplementary Figure 4.
Discharge voltage profiles for the 1st and 50th cycle in **a**) 0SL, and **b**) 70SL.

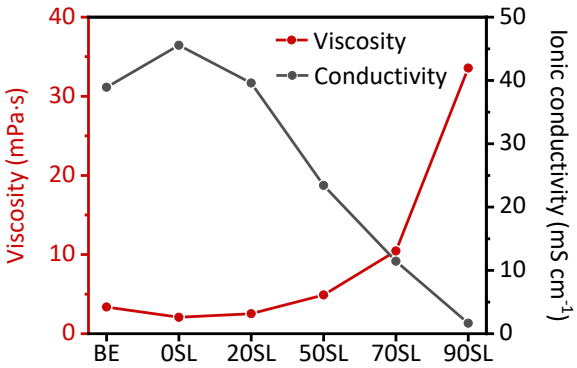

Supplementary Figure 5.
Ionic conductivities and viscosities of electrolytes with different weight percentages of sulfolane.

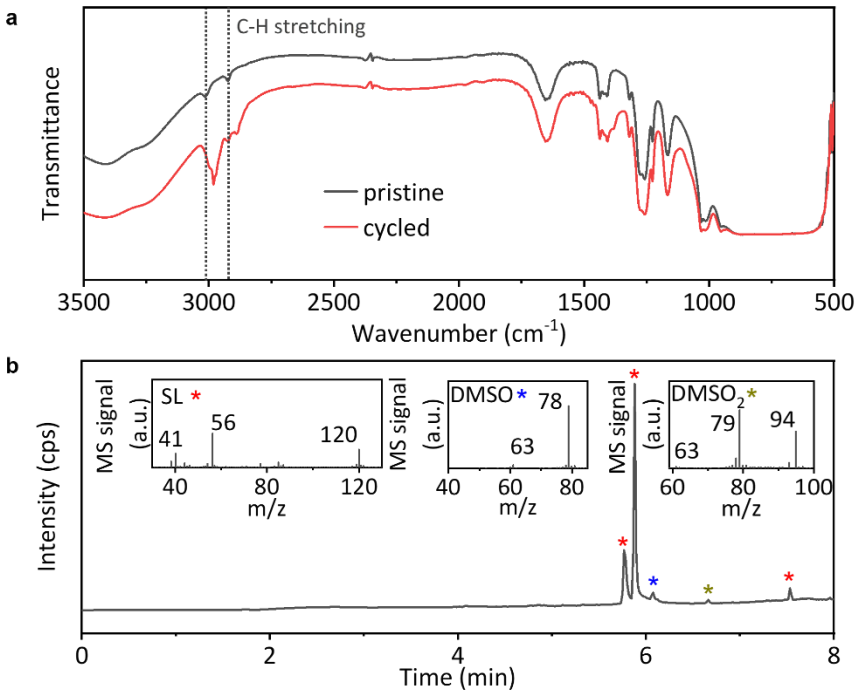

Supplementary Figure 6.

a) FTIR spectra of the pristine 70DMSO electrolyte and cycled electrolyte show oxidation of DMSO after charge. The shift and increased intensity of the symmetric and asymmetric C-H stretching modes indicate the oxidation of DMSO to $DMSO_2$. b) Gas chromatography-mass spectrometry (GC-MS) analysis of the electrolyte upon charge show the presence of $DMSO_2$. No signals appear before the organic species, eliminating the possibility of a chlorine oxidation side reaction.

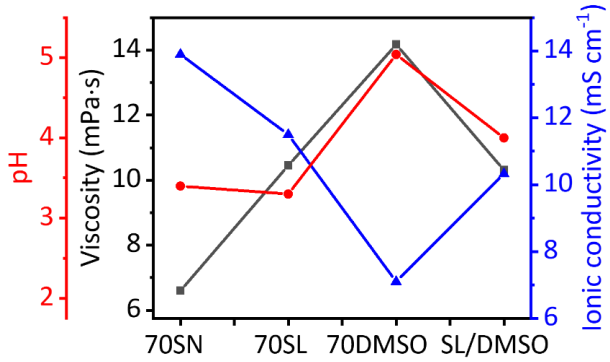

Supplementary Figure 7.
Measured viscosity, ionic conductivity, and pH values of the different electrolytes.

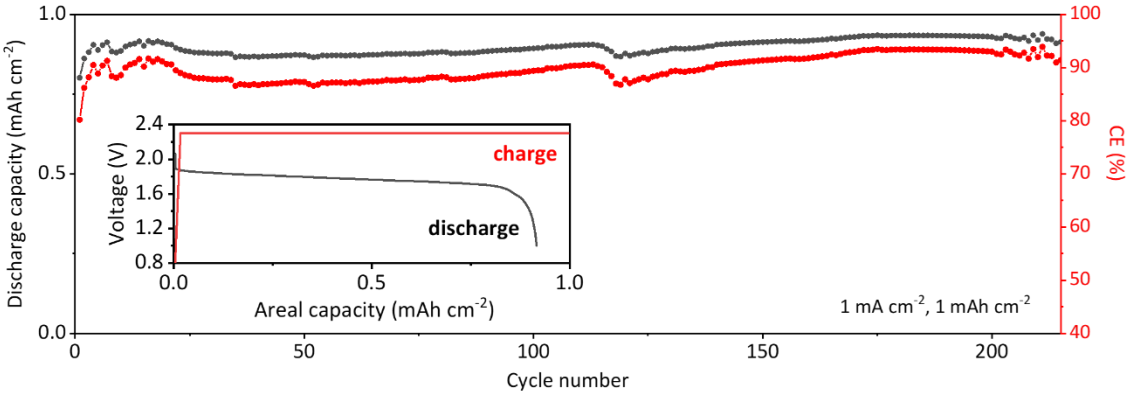

Supplementary Figure 8.
Voltage profile, cycling performance and Coulombic efficiency of the full $Zn^{2+}/Zn||MnO_2/Mn^{2+}$ cell in the SL/DMSO ternary electrolyte, charged to 1 mAh·cm^{-2} and discharged at 1 mA·cm^{-2} (C rate).

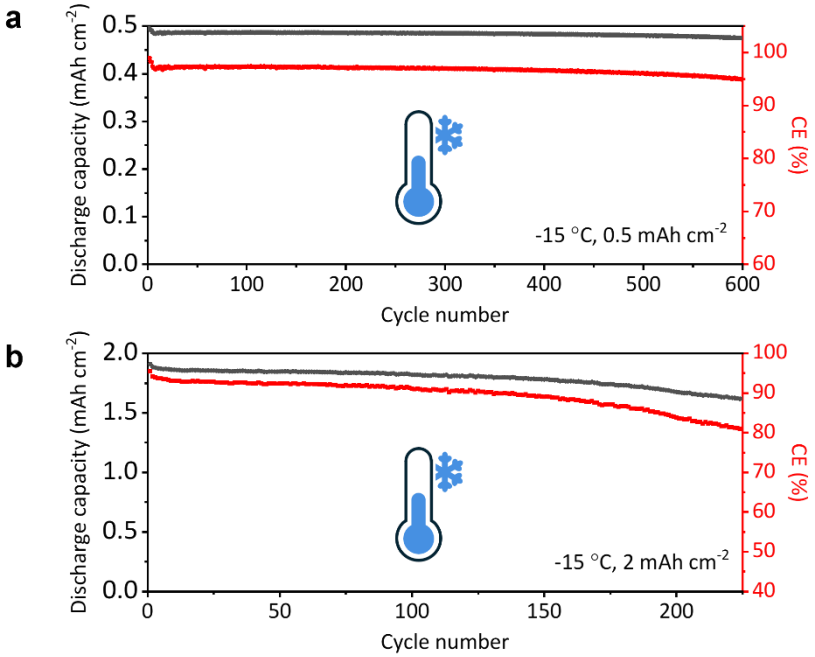

Supplementary Figure 9.

Electrochemical performance at low temperature. a) Voltage profiles and Coulombic efficiency of full cell in SL/DMSO mixed system charged to 0.5 mAh·cm^{-2} and discharged at 5 mA·cm^{-2} at -15℃. **b)** Voltage profiles and Coulombic efficiency of the SL/DMSO cell at 2 mAh·cm^{-2} and 12 mA·cm^{-2} at -15℃.

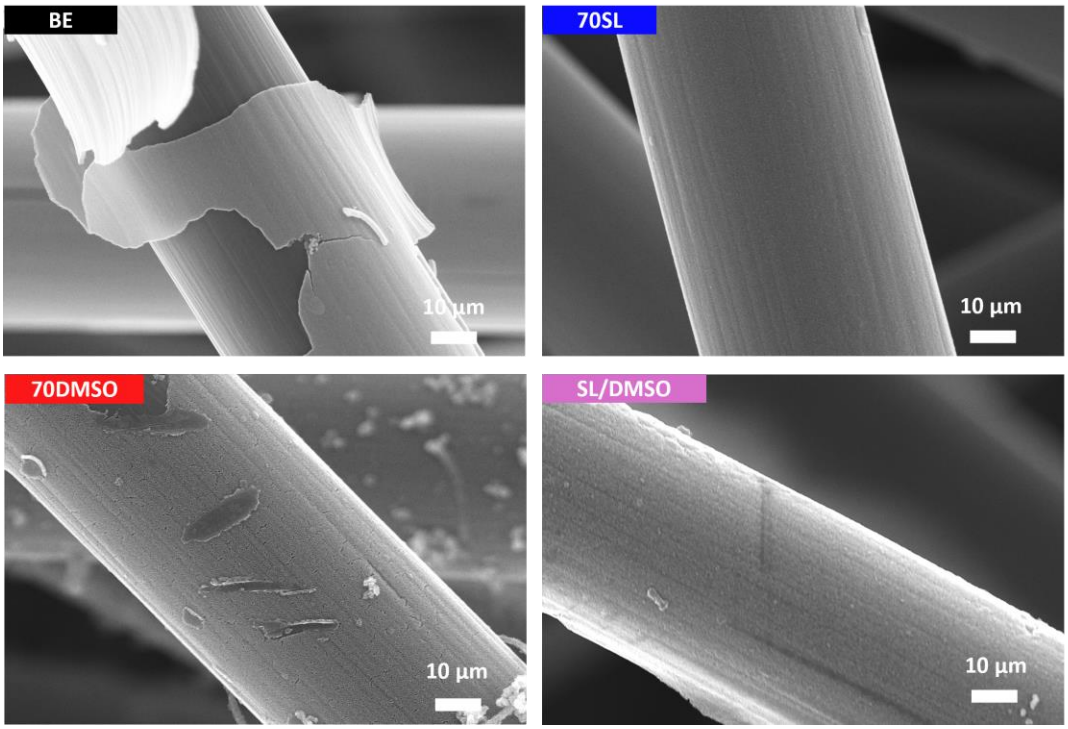

Supplementary Figure 10.
Scanning electron microscopy (SEM) images for 0.5 mAh·cm^{-2} MnO_2 deposited in the BE, 70SL, and 70DMSO electrolytes.

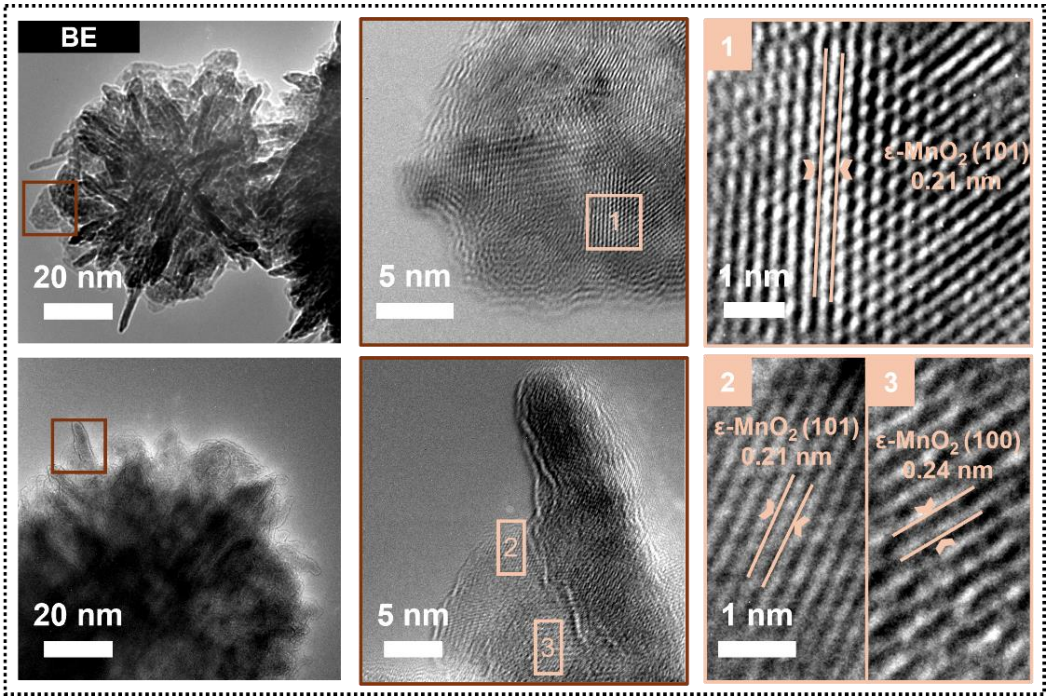

Supplementary Figure 11.
Cryogenic electron microscopy (Cryo-EM) images for MnO_2 deposited in the BE electrolyte.

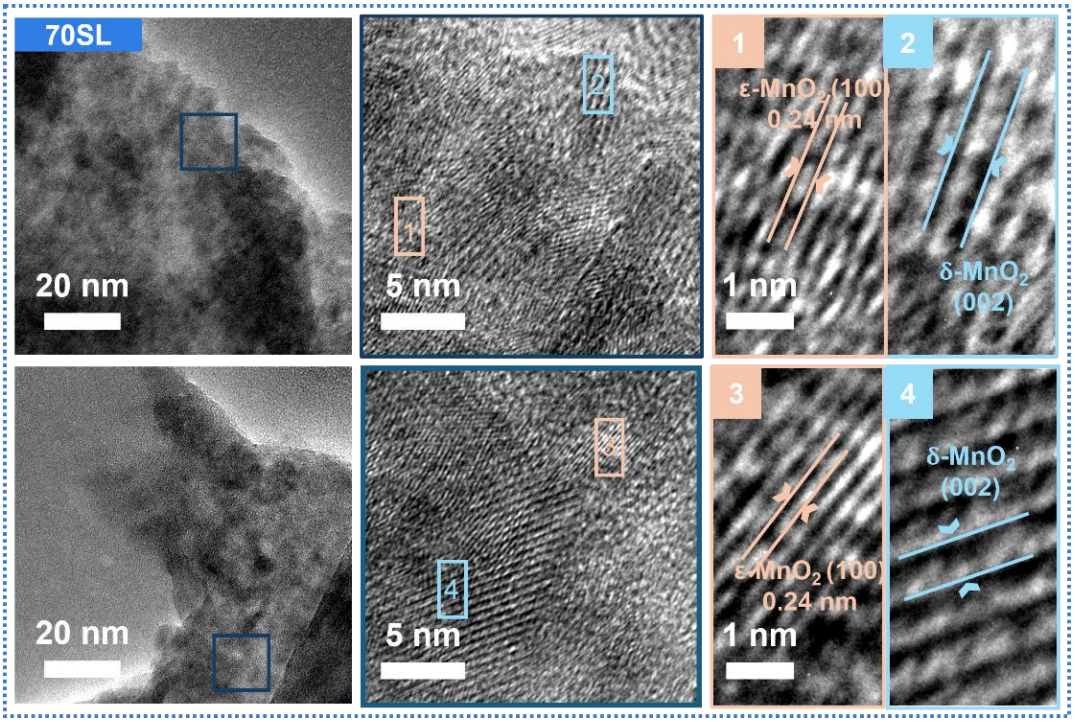

Supplementary Figure 12.
Cryo-EM images for MnO_2 deposited in the 70SL electrolyte.

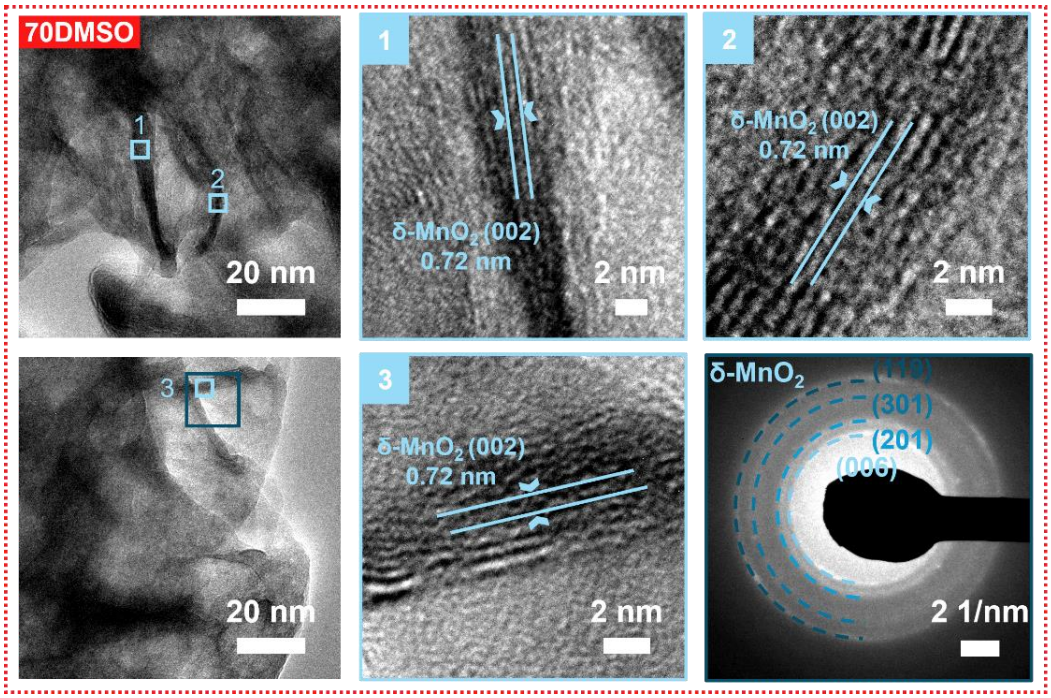

Supplementary Figure 13.
Cryo-EM images and selected area electron diffraction (SAED) pattern for MnO_2 deposited in the 70DMSO electrolyte.

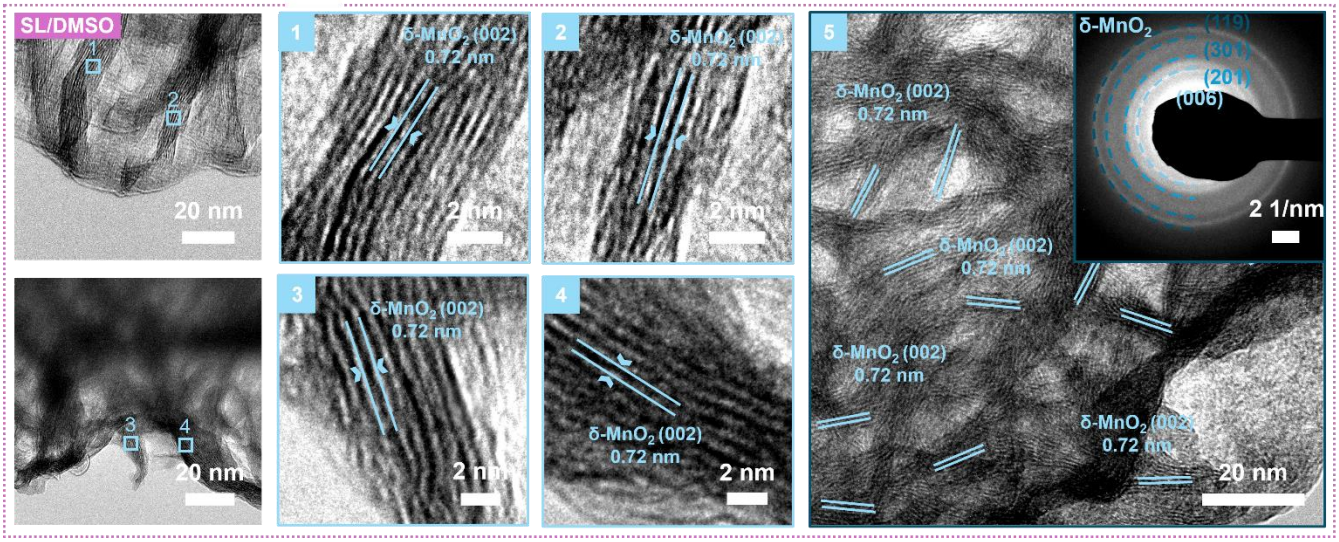

Supplementary Figure 14.
Cryo-EM images and SAED pattern for MnO_2 deposited in the ternary electrolyte SL/DMSO.

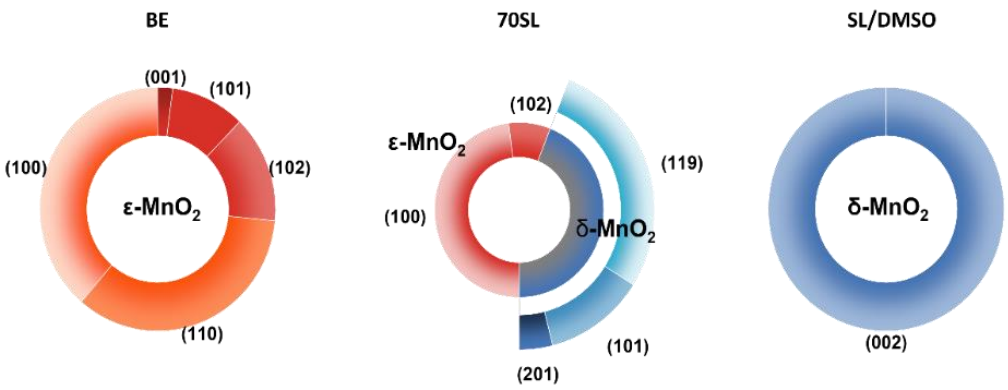

Supplementary Figure 15.
HRTEM statistics for phase analysis of MnO_2 in different electrolytes, collecting over 50 independent lattice spacings measurements per electrolyte. To avoid overrepresentation, we skipped adjacent regions along one fringe and prioritized assignments based on lattice planes with higher intensity in the corresponding XRD patterns.

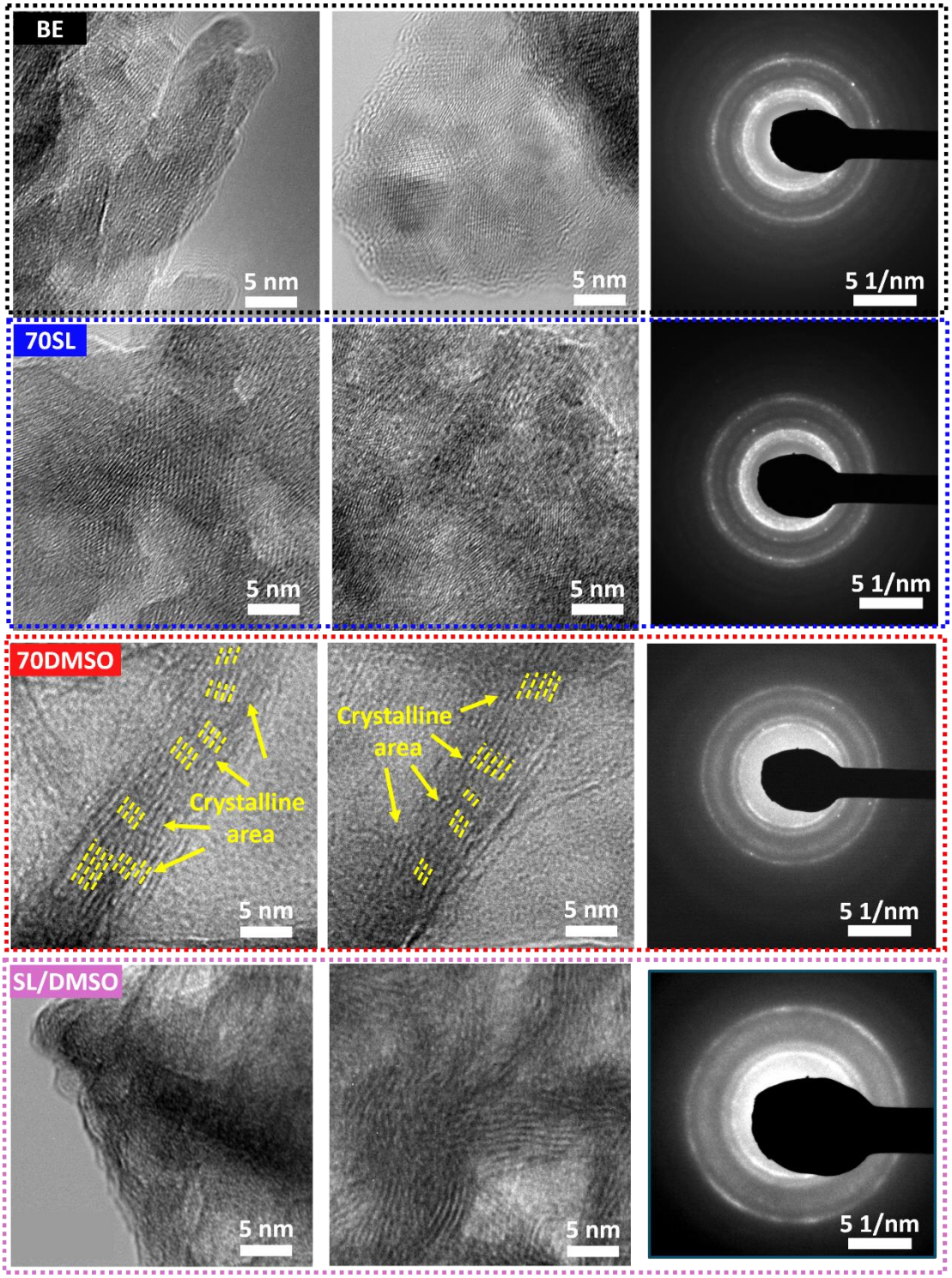

Supplementary Figure 16.
Cryo-EM images and SAED patterns showing crystallinity of MnO_2 deposited in 70DMSO and SL/DMSO with limited crystallinity and broadened SAED pattern.

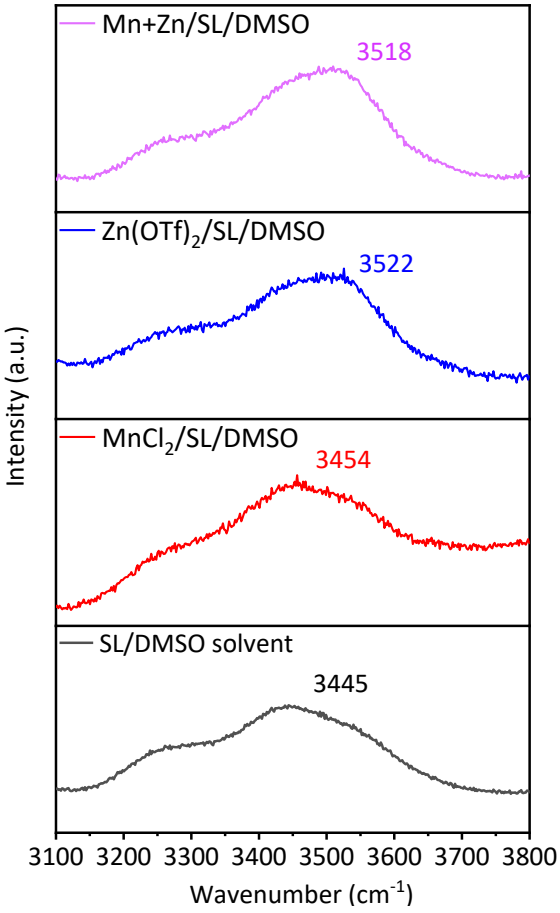

Supplementary Figure 17.
Raman spectra of the water -OH stretching band for various SL/DMSO solutions.

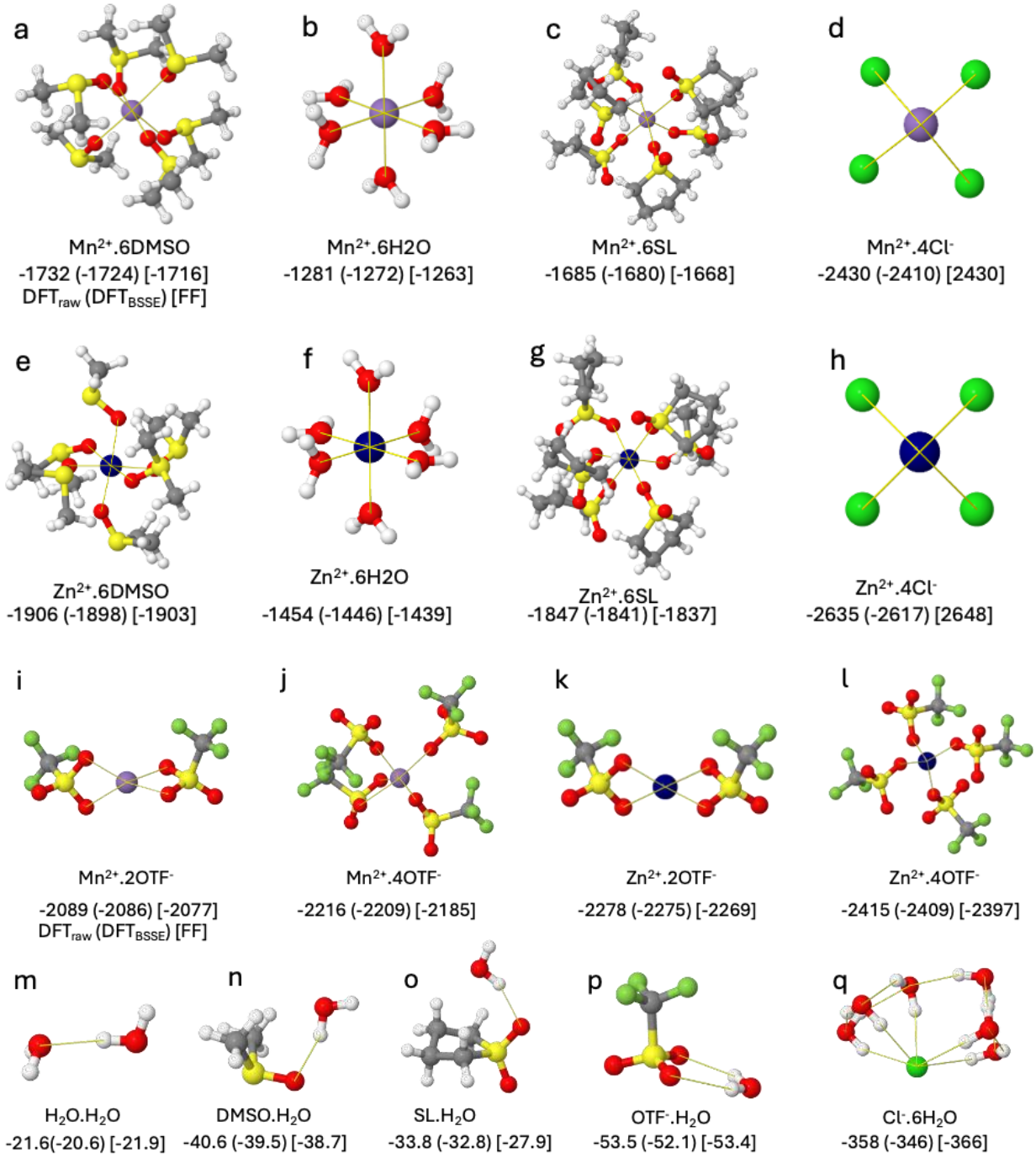

Supplementary Figure 18.
Binding energies from ωb97xd/def2-QZVP DFT calculations before and after basis set superposition energy correction (DFT_{BSSE}) and molecular mechanics using the developed APPLE&P force field shown within square backets [FF] in kJ mol^{-1}.

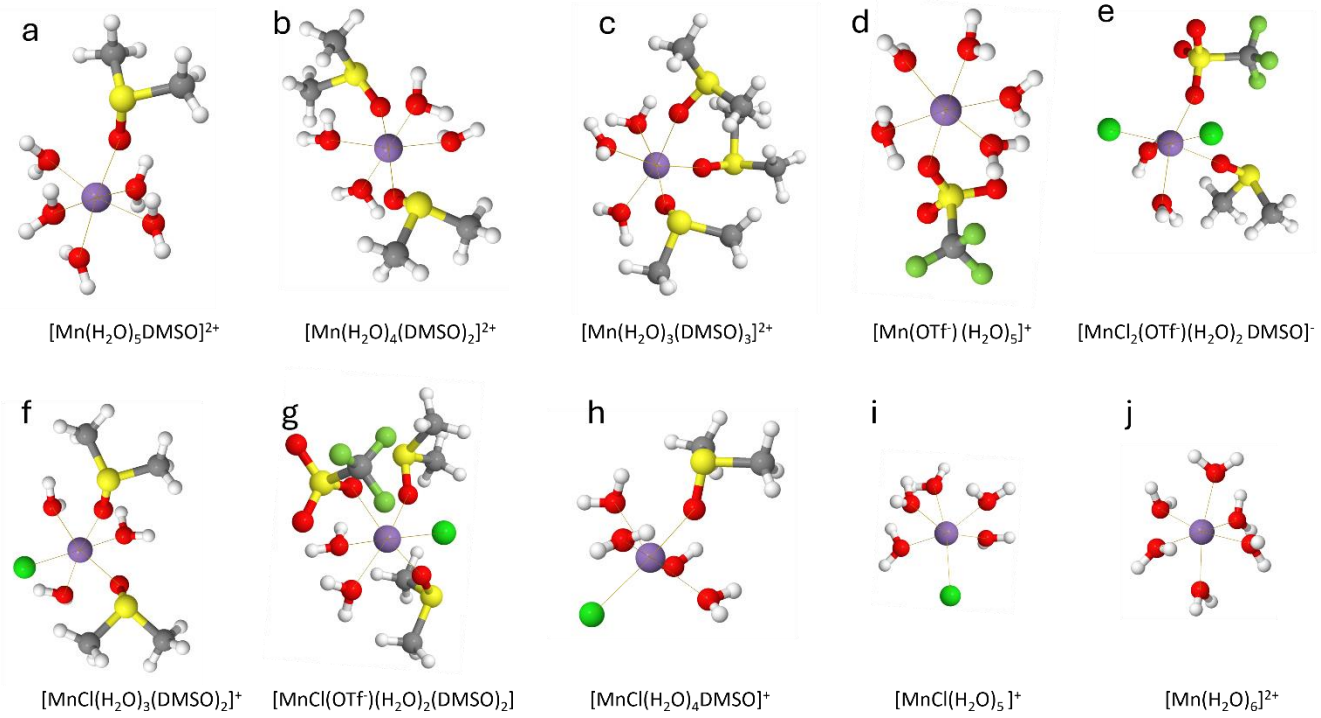

Supplementary Figure 19.
Representative Mn^{2+} clusters in the SL/DMSO model.

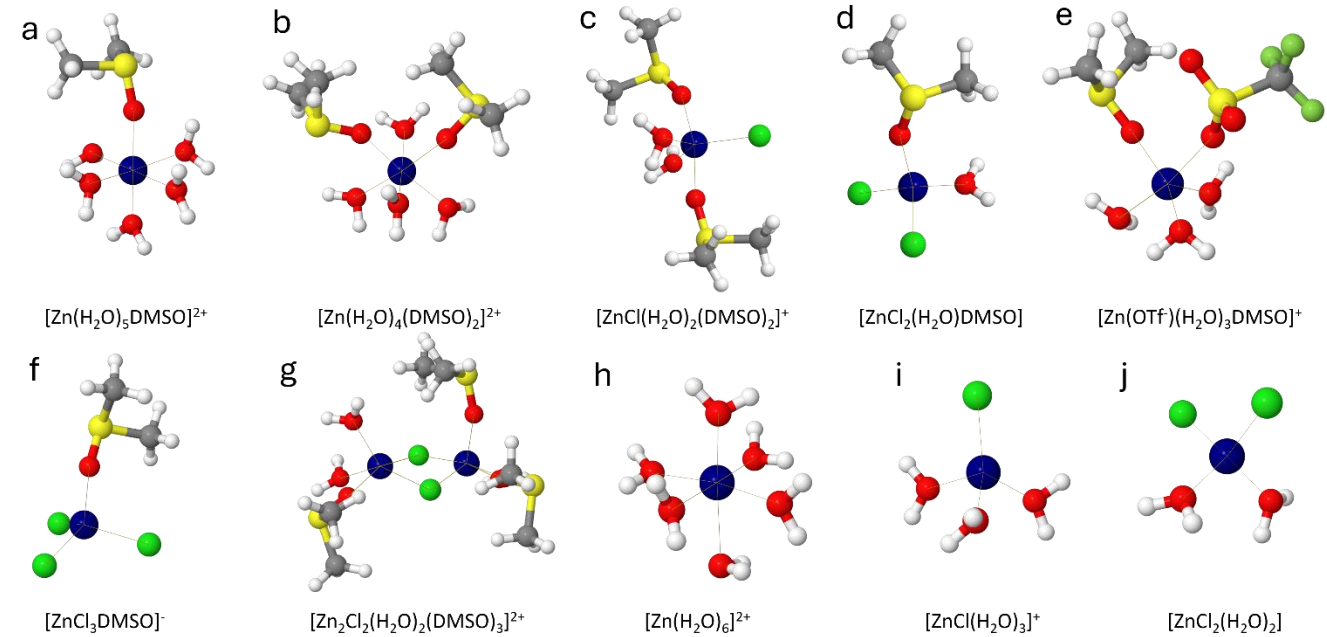

Supplementary Figure 20.
Representative Zn^{2+} clusters in the SL/DMSO model.

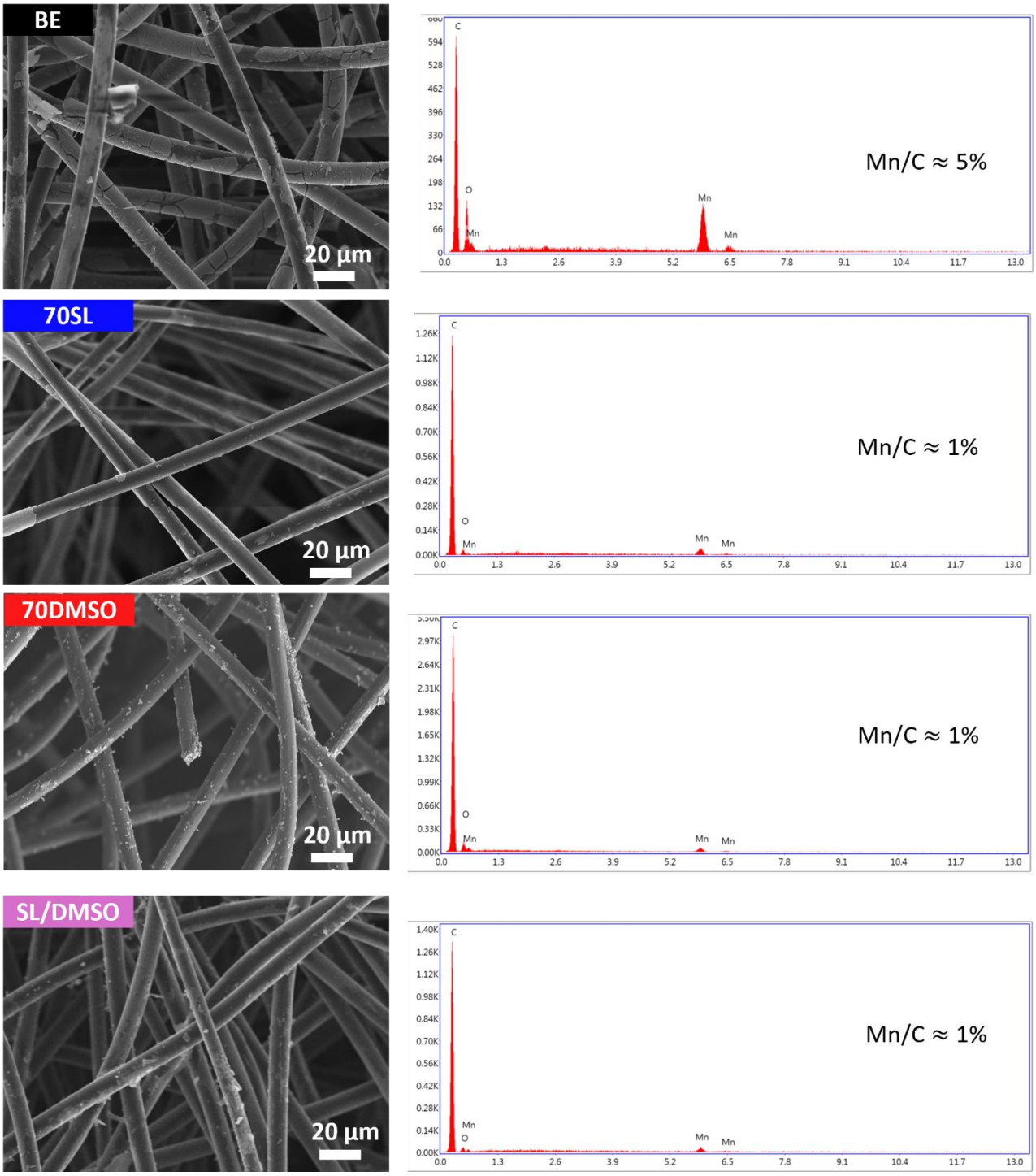

Supplementary Figure 21.
Energy-dispersive X-ray spectroscopy (EDS) analysis of discharged cathodes after 10 cycles at 0.5 mAh·cm^{-2} in the BE, 70DMSO, 70SL and SL/DMSO electrolytes.

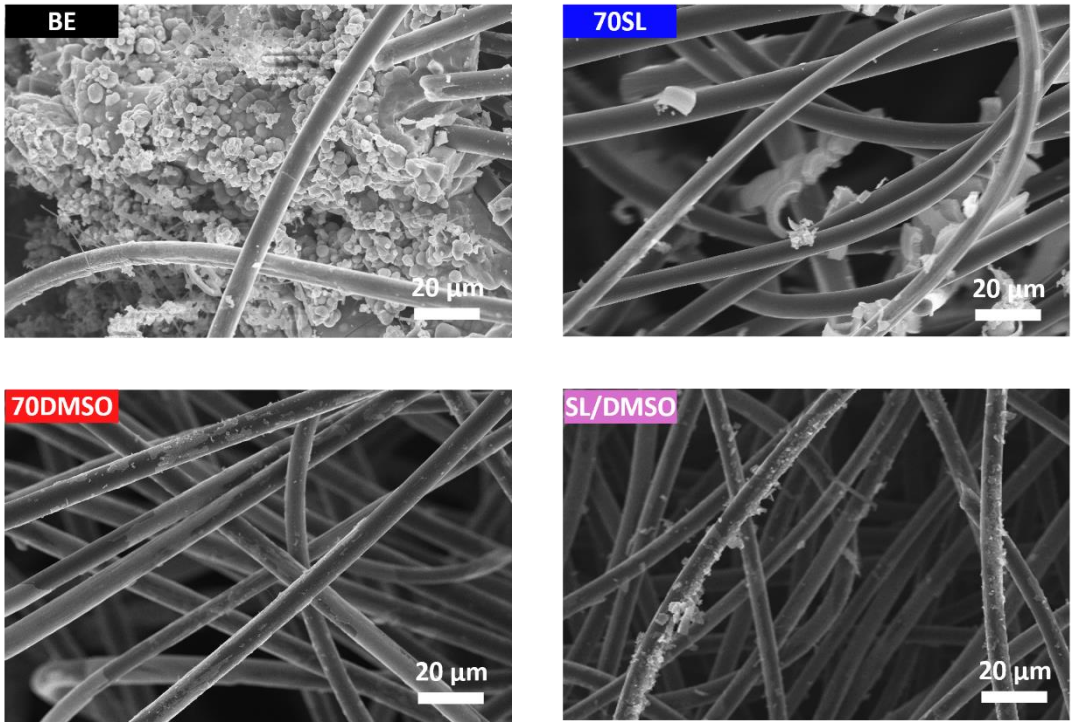

Supplementary Figure 22.
SEM images of a cathode cycled at 2 $mAh \cdot cm^{-2}$ for 20 cycles in the BE, 70DMSO, 70SL and SL/DMSO electrolytes.

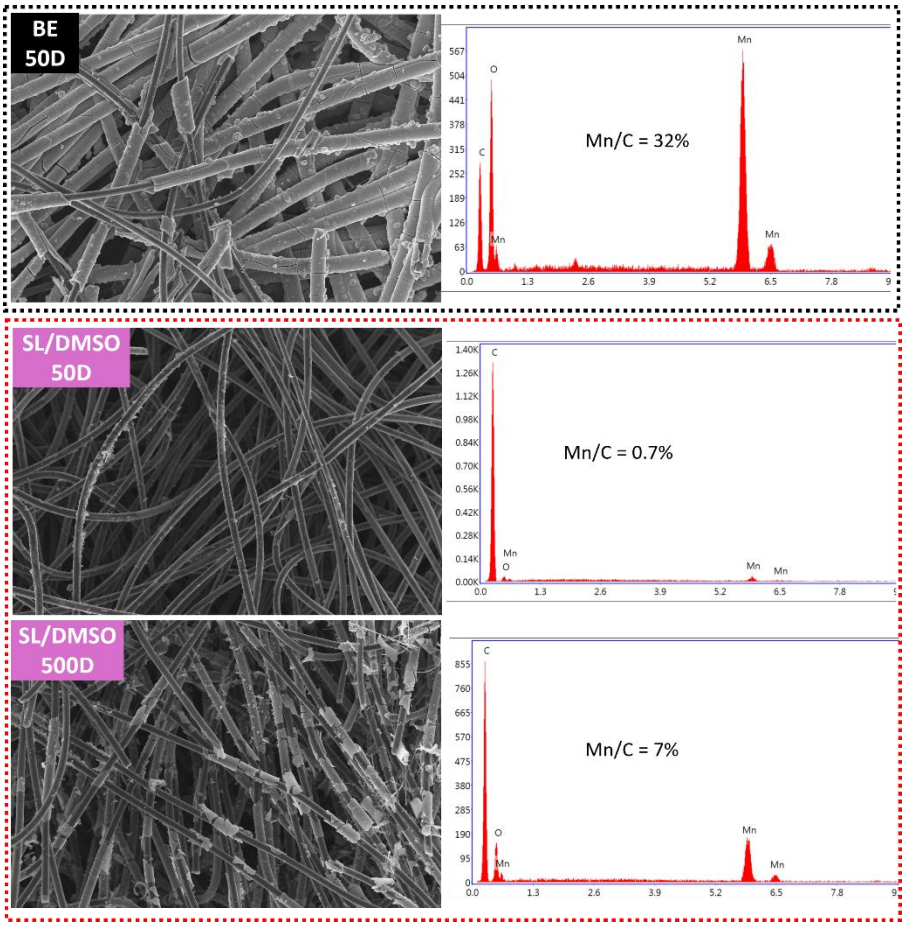

Supplementary Figure 23.
SEM images of cathodes cycled at 0.5 mAh·cm^{-2} for 50 (50D) and 500 cycles (500D) in the ternary electrolyte SL/DMSO and in the BE.

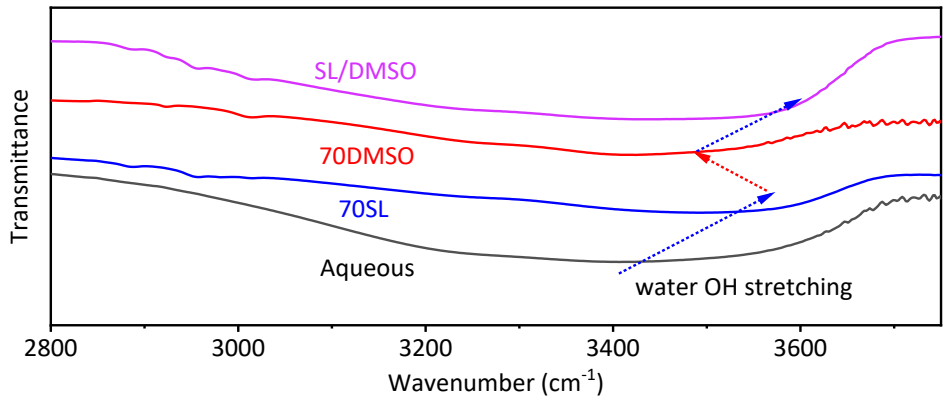

Supplementary Figure 24.
FTIR spectra of SL/DMSO, 70SL, 70DMSO, and the aqueous electrolyte in the water -OH stretching region.

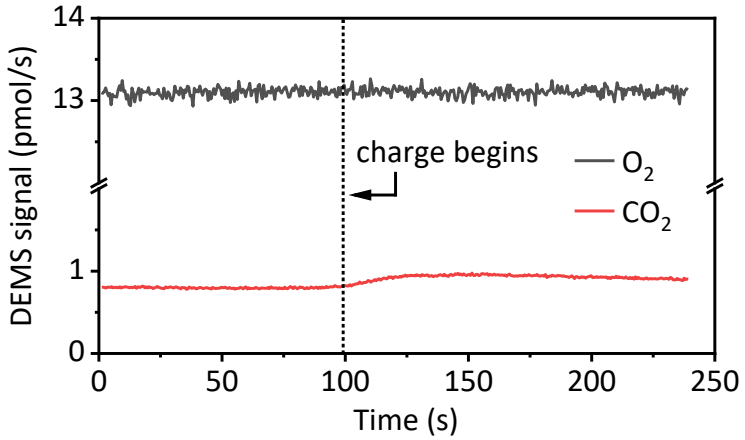

Supplementary Figure 25.
Differential electrochemical mass spectrometry (DEMS) measurements of O_2 and CO_2 signals during cell charging at 2.9 V vs. Zn^{2+}/Zn in 70DMSO.

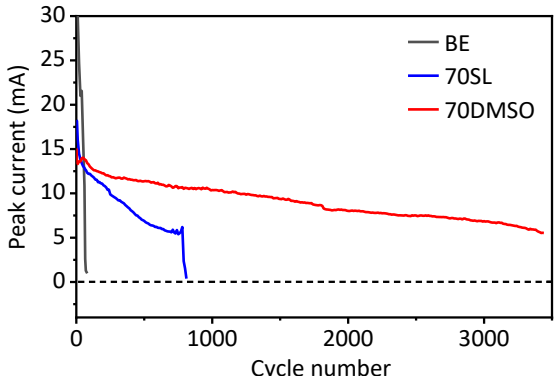

Supplementary Figure 26.
The peak current response during constant voltage charging in different electrolytes.

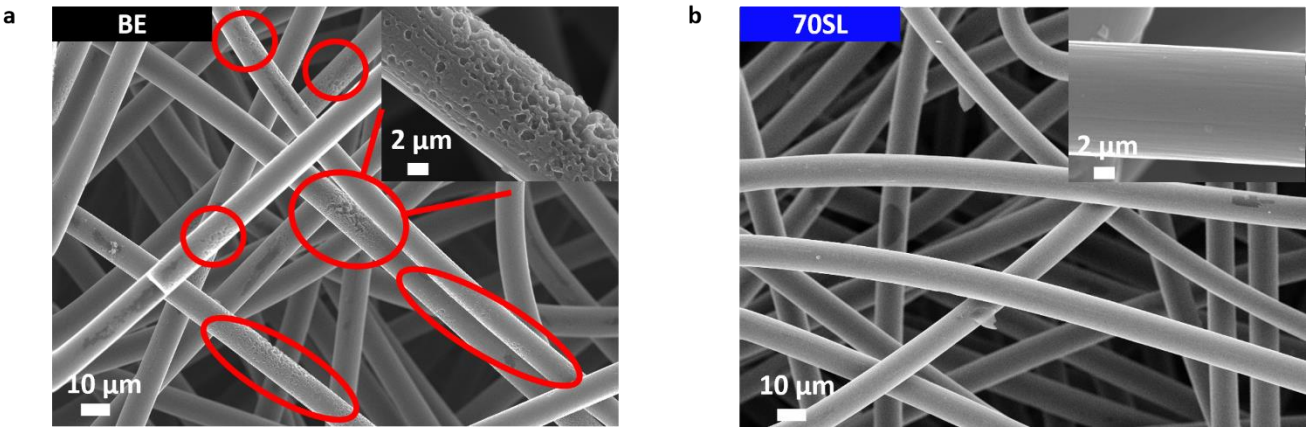

Supplementary Figure 27.
SEM images of cathodes after the first charge in the **a)** BE and **b)** 70SL electrolytes. The highly irregular, patchy oxide deposition in the BE is highlighted by red ellipses.

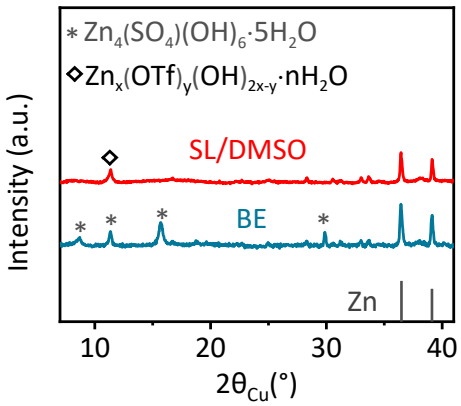

Supplementary Figure 28.

X-ray diffraction (XRD) patterns of Zn deposited on the Cu anode after 2 cycles at 4 mAh·cm^{-2} and 2 mA·cm^{-2} in SL/DMSO and the BE. SL/DMSO shows reduced $Zn_x(OTf)_y(OH)_{2x-y}·nH_2O$ formation compared to $Zn_4(SO_4)(OH)_6·5H_2O$ in the BE.

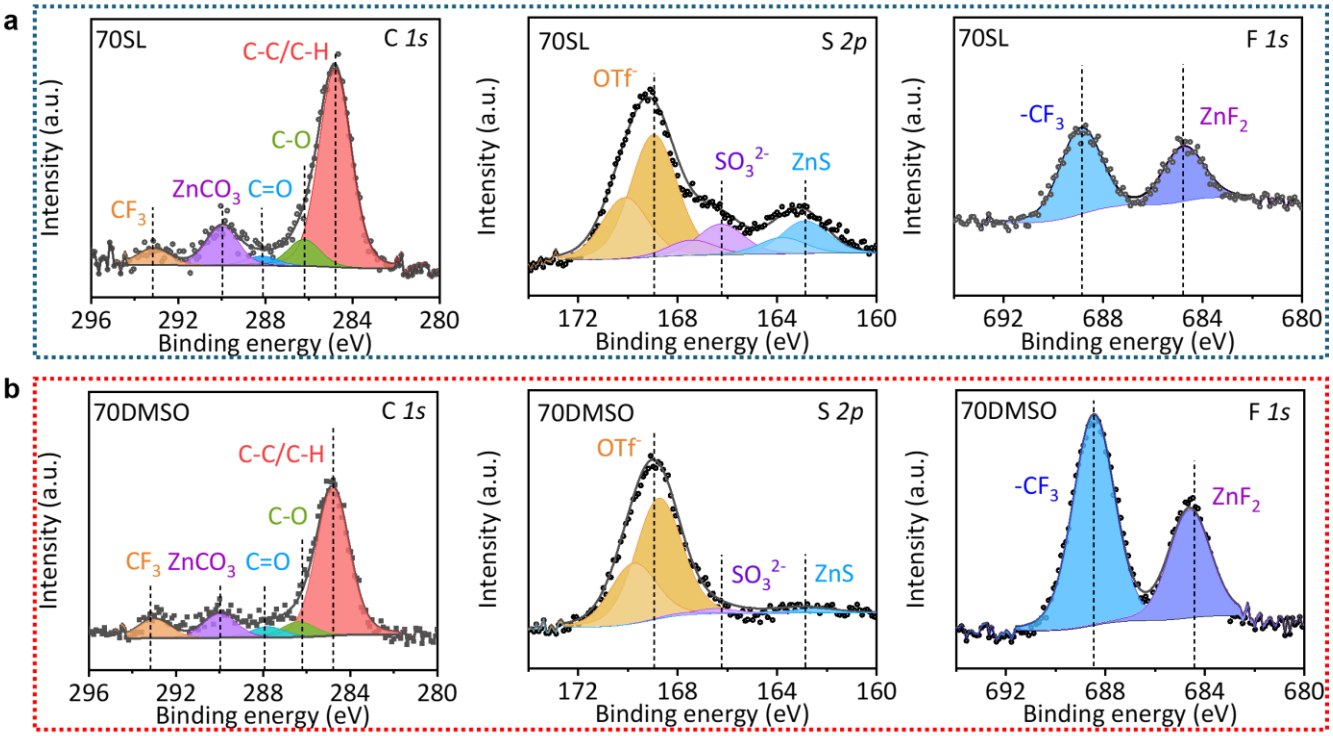

Supplementary Figure 29.

XPS C *1s*, S *2p*, and F *1s* spectra of Cu electrodes with deposited Zn after 2 cycles at 2 mA·cm^{-2} with 4 mAh·cm^{-2} in a) 70SL and b) 70DMSO.

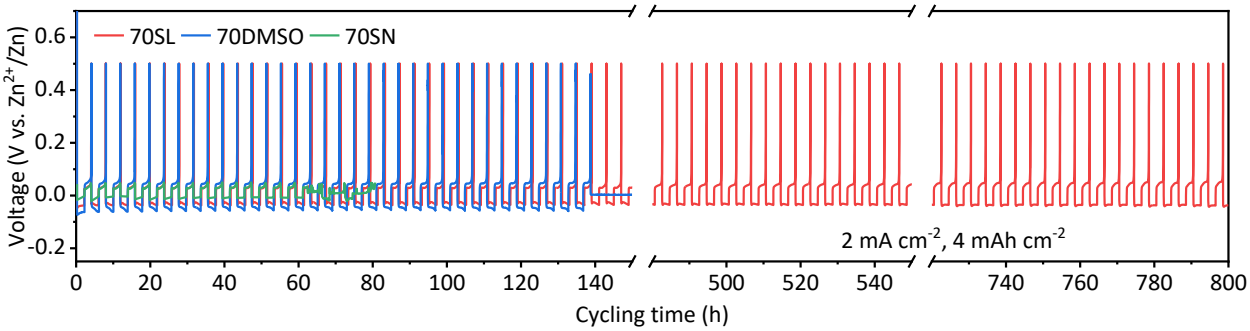

Supplementary Figure 30.
Galvanostatic cycling profiles of Zn||Cu cell in individual eutectic electrolytes of 70SL, 70DMSO, and 70SN at 2 mA·cm^{-2} with a capacity of 4 mAh·cm^{-2}. 70SN exhibits the shortest cycling lifetime, while 70SL shows the most stable cycling with a Zn anode.

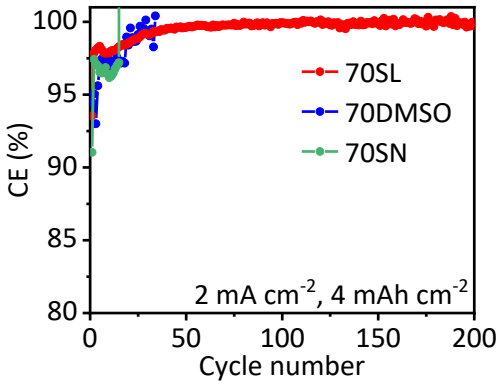

Supplementary Figure 31.
Coulombic efficiency of Zn||Cu cells in individual eutectic electrolytes: 70SL, 70DMSO, and 70SN.

Supplementary Tables:

Supplementary Table 1. Energy density of Zn-MnO_2 full cell.

Capacity (mAh)	Cathode mass (mg)	Anode mass (mg)	Average voltage (V)	Energy density (Wh/kg)
1.424	12	5	2	167

Supplementary Table 2. Active mass change at the cathode in different electrolytes.

	Δm after 1st charge (1C) (mg/cm^2)	Δm after 1st discharge (1D) (mg/cm^2)	Δm after 50th discharge (50D) (mg/cm^2)
BE	+3.21	+0.96	+16.94
SL/DMSO	+3.09	+0.17	+1.30

The cathodes cycled at 2 mAh/cm^2 were washed with DI water and ethanol and dried in 60℃ oven overnight before weighing. The mass change after discharge shows that residual MnO_2 accumulation is severe in the BE, while greatly reduced in the hybrid electrolyte.

Supplementary Table 3. The free energies(ΔG) at 298.15 K (ΔG) for the Mn^{2+} and Zn^{2+} solvation by DMSO, H_2O and SL solvents or coordination by $4Cl^-$ or $4OTf^-$ anions. All solvates were immersed in implicit solvent described by SMD (ε=20) model.

	Free Energy ΔG (kJ mol^{-1})
Zn^{2+}.6DMSO	-1954
Zn^{2+}.6H_2O	-1926
Zn^{2+}.6SL	-1837
Zn^{2+}.4Cl^-	-2069
Zn^{2+}.4OTf^-	-1936
Mn^{2+}.6DMSO	-1792
Mn^{2+}.6H_2O	-1760
Mn^{2+}.6SL	-1670
Mn^{2+}.4Cl^-	-1846
Mn^{2+}.4OTf^-	-1686

Supplementary Table 4. The free energies for cation-Cl contact ion pair formation.

	Free Energy ΔG (kJ mol^{-1})
MnCl in DMSO	-32
MnCl in H_2O	-40
MnCl in SL	-73
ZnCl in DMSO	-33
ZnCl in H_2O	-62
ZnCl in SL	-70

Supplementary Note 1. Electrolyte Modeling

The relative affinity of DMSO, SL, water and Cl^-/OTf^- anions to Mn^{2+} and Zn^{2+} were investigated in the cluster-continuum with density functional theory (DFT) calculations performed using the gaussian g16 C.02 package[1] and molecular dynamics (MD) simulations.

In the cluster-continuum DFT calculations, the cation binding free energies to solvents and anions were calculated relative to the isolated Zn^{2+} and Mn^{2+} cations in the gas-phase, and DMSO, SL solvents and Cl^- and OTf^- anions in an implicit solvent are represented using a universal solvation model based on solute electron density (SMD) with dielectric constant of 20 for dimethyl ketone.[2] To minimize the inaccuracies of the implicit solvent model, the first coordination shell of cations was considered explicitly - that is, by including six solvents or four anions in calculations. To account for the hydrogen bonding within the water network, the water prism $(H_2O)_6$ structure was used to represent water instead of an isolated water molecule. The resulting Mn^{2+} and Zn^{2+} solvation free energies from ωb97xd/def2-TZVP are shown in **Supplementary Table 3**. The absolute values for the Zn^{2+} and Mn^{2+} cation solvation energies follow the order Cl^- > DMSO > OTf^- > H_2O > SL, indicating the salt dissociation trends in different solvents. This simple model, however, does not explicitly consider the anion – water hydrogen bonding because it utilized the implicit solvent SMD model to estimate the dissociated Cl^- and OTf^- energies. The explicit hydrogen bonding between water and Cl^- was included by using the $Cl^-(H_2O)_7$ complexes instead of the isolated Cl^- in calculations of the contact ion pair (CIP) formation shown in **Supplementary Table 4**. The free energies of contact ion pair formation were obtained from the following reaction

$M^{2+}(Solv)_5Cl^- \rightarrow M^{2+}(Solv)_6 + Cl^-$ or $Cl^-(H_2O)_7$ in the case of water,

where M^{2+} denotes a metal cation Mn^{2+} or Zn^{2+} and Solv denotes DMSO, SL or H_2O. An explicit inclusion of hydrogen bonding in the first solvation shell of Cl^- in water H_2O results in the CIP formation energies following the order SL > H_2O > DMSO for both Mn^{2+} and Zn^{2+}. Interestingly, ZnCl CIP formation in H_2O is more favorable than MnCl CIP formation in water, while ZnCl vs. MnCl CIP formation were similar in DMSO and SL.

A many-body polarizable APPLE&P force field[3-5] was extended to Mn^{2+}, Cl^- and DMSO by refitting the repulsion interaction to fit the binding energy from ωb97xd/def2-QZVP DFT calculations for $Cl^-.H_2O$ paths and clusters shown in **Supplementary Fig. 24**. The cation – solvent binding energies from the developed force field were often ~10 kJ mol^{-1} lower than ωb97xd/def2-QZVP DFT results, in accord with previous force fields for lithium-based electrolytes.[6] Selective benchmarking for $Zn^{2+}(H_2O)_2$ binding energy yielded values of -796 kJ mol^{-1} (-793 kJ mol^{-1} after BSSE correction) for ωb97xd/def2-QZVP DFT, which is slightly higher than the complete basis set (CBS) extrapolation after BSSE correction of -785 kJ mol^{-1} for the Møller–Plesset perturbation theory second order (MP2) with the frozen core and -791 kJ mol^{-1} for MP2/CBS with full electron correlations. Coupled cluster including triplets CCSD(T)/aug-cc-pvQz yielded a value of 776 kJ mol^{-1} also indicating that ωb97xd/def2-QZVP DFT might slightly overestimate binding energy of the cations to solvents. For the $Cl^-(H_2O)_6$

ωb97xd/def2-QZVP DFT slightly underestimate the binding energy compared to RI-CCSD(T)/CBS results of -361.7 kJ mol^{-1} reported by Lao and Herbert.[2] Force field results for $Cl^-(H_2O)_6$ are closer to RI-CCSD(T)/CBS than to ωb97xd/def2-QZVP DFT.

In MD simulations, a time reversible (RESPA) integrator with three-time steps was used: i) bonds and angles to the forces were calculated at any 0.5 femtoseconds (fs), ii) dihedrals and non-bonded forces within a 7 Å cut-off was updated at any 1.5 fs, and iii) the remainder of the forces (reciprocal space Ewald using $k=8^3$ vectors) and non-bonded forces within a 18-24 Å cut-off was updated at any 3 fs. Ewald was used for permanent charge interactions with permanent charges and induced dipoles, while induced dipole – induced dipole interactions were calculated in real space. A Nose-Hoover thermostat was used for temperature control with the associated frequency of 0.01 fs^{-1}. The induced dipoles (μ) were found self-consistently at each 3fs timestep with the tolerance of $\mu^2 < 1*10^{-12}$ $(e*Å)^2$.

MD simulations were performed for the target electrolyte containing 490 DMSO, 425 SL, 2130 SL, 64 $MnCl_2$ and 128 $Zn(OTf)_2$ in a simulation cell after quick validation performed on 4 m $Mn(OTf)_2$ and 4 m $Zn(OTf)_2$ in water (96 salts + 1331 waters) and $ZnCl_2$ in $8H_2O$ (320 $ZnCl_2$ in 2560 waters). MD simulations of 4 m $Mn(OTf)_2$ and 4 m $Zn(OTf)_2$ in water at 363 K performed for 35 ns yielded Mn^{2+} and Zn^{2+} coordination by 5.85 – 5.9 waters and less than 0.1 oxygens of OTf^- indicating near complete dissociation of salt in accord with previous studies of 4 m $Zn(OTf)_2$ using Raman and MD simulations.[4] 25 ns MD simulations of $ZnCl_2$:$8H_2O$ at 363 K yielded Zn^{2+} coordinated by 3.9 H_2O and 1.2 Cl^- in accord with the recent coordinated experimental and MD simulation study using machine learned – DFT based force field.[4]

Three replicas using different states of salt aggregation and solvent coordination of the DMSO-SL-H_2O: $Zn(OTf)_2$/$MnCl_2$ were setup and equilibrated for 8 ns at 393 K followed by 6 ns simulations at 363 K. Radial distribution functions were calculated over the last 1 ns run at 363 K. We note that we used temperatures as low as possible to obtain convergence in a reasonable time frame. MD simulations at a more realistic temperature of 300 K are hard to converge due to the extremely long relaxation time of DMSO. We acknowledge the limitation of this model, but it still provides valuable information.

References

1. Frisch, M. J. T., G. W.; Schlegel, H. B.; Scuseria, G. E.; Robb, M. A.; Cheeseman, J. R.; Scalmani, G.; Barone, V.; Petersson, G. A.; Nakatsuji, H.; Li, X.; Caricato, M.; Marenich, A. V.; Bloino, J.; Janesko, B. G.; Gomperts, R.; Mennucci, B.; Hratchian, H. P.; Ortiz, J. V.; Izmaylov, A. F.; Sonnenberg, J. L.; Williams-Young, D.; Ding, F.; Lipparini, F.; Egidi, F.; Goings, J.; Peng, B.; Petrone, A.; Henderson, T.; Ranasinghe, D.; Zakrzewski, V. G.; Gao, J.; Rega, N.; Zheng, G.; Liang, W.; Hada, M.; Ehara, M.; Toyota, K.; Fukuda, R.; Hasegawa, J.; Ishida, M.; Nakajima, T.; Honda, Y.; Kitao, O.; Nakai, H.; Vreven, T.; Throssell, K.; Montgomery, J. A., Jr.; Peralta, J. E.; Ogliaro, F.; Bearpark, M. J.; Heyd, J. J.; Brothers, E. N.; Kudin, K. N.; Staroverov, V. N.; Keith, T. A.; Kobayashi, R.; Normand, J.; Raghavachari, K.; Rendell, A. P.; Burant, J. C.; Iyengar, S. S.; Tomasi, J.; Cossi, M.; Millam, J. M.; Klene, M.; Adamo, C.; Cammi, R.; Ochterski, J. W.; Martin, R. L.; Morokuma, K.; Farkas, O.; Foresman, J. B.; Fox, D. J. Gaussian, Inc., Wallingford CT, 2016. Gaussian 16, Revision C.02, Gaussian, Inc., Wallingford CT. 2019.

2. Lao, K. U.; Herbert, J. M. An improved treatment of empirical dispersion and a many-body energy decomposition scheme for the explicit polarization plus symmetry-adapted perturbation theory (XSAPT) method. *The Journal of Chemical Physics* **2013**, *139* (3). DOI: 10.1063/1.4813523 (acccessed 9/2/2025).

3. Borodin, O. *APPLE&P (Atomistic Polarizable Potential for Liquids, Electrolytes and Polymers). rev 1e www.wasatchmolecular.com*. 2009. (accessed 2nd September 2025)

4. Cao, L.; Li, D.; Pollard, T.; Deng, T.; Zhang, B.; Yang, C.; Chen, L.; Vatamanu, J.; Hu, E.; Hourwitz, M. J.; Ma, L.; Ding, M.; Li, Q.; Hou, S.; Gaskell, K.; Fourkas, J. T.; et al. Fluorinated interphase enables reversible aqueous zinc battery chemistries. *Nature Nanotechnology* **2021**, *16*, 902–910. DOI: 10.1038/s41565-021-00905-4.

5. Alvarado, J.; Schroeder, M. A.; Zhang, M.; Borodin, O.; Gobrogge, E.; Olguin, M.; Ding, M. S.; Gobet, M.; Greenbaum, S.; Meng, Y. S.; Xu, K. A carbonate-free, sulfone-based electrolyte for high-voltage Li-ion batteries. *Materials Today* **2018**, *21* (4), 341-353. DOI: https://doi.org/10.1016/j.mattod.2018.02.005.

6. Borodin, O.; Smith, G. D. Quantum Chemistry and Molecular Dynamics Simulation Study of Dimethyl Carbonate: Ethylene Carbonate Electrolytes Doped with LiPF6. *J. Phys. Chem. B* **2009**, *113* (6), 1763-1776. DOI: 10.1021/jp809614h.